Adaptive camera calibration for a focus adjustable liquid lens in fiber optic endoscopy

Hinz, Lennart, Kästner, Markus, Reithmeier, Eduard

SPIE.

Adaptive Camera Calibration for a Focus Adjustable Liquid Lens in Fiber Optic Endoscopy

Lennart Hinz[a], Markus Kästner[a], and Eduard Reithmeier[a]

[a]Institute of Measurement and Automatic Control, An der Universität 1, Garbsen, Germany

ABSTRACT

Benefiting from recent innovations in the smartphone sector, liquid optics in very compact designs have been cost-effectively introduced to the market. Without mechanical actuation, a focus variation can be adjusted within fractions of a second by curving a boundary layer between two liquids by applying a pulse width or amplitude modulated potential. Especially in the field of endoscopy, these innovative optical components open up many application possibilities. Conventional, mechanical zoom lenses are not very common in endoscopy and can only be miniaturized at considerable effort due to the necessary actuation and the complex design. In addition, the mechanical response is slow, which is a particular disadvantage in hand-held operation. A calibrated camera provides a two-dimensional camera pixel translated into a three-dimensional beam and, together with distortion correction enables the extraction of metric information. This approach is widely used in endoscopy, for example, to measure objects in the scene or to estimate the camera position and derive a trajectory accordingly. This is particularly important for triangulation-based 3D reconstruction such as photogrammetry. The use of liquid lenses requires a new data set with an adapted camera calibration for each focus adjustment. In practice, this is not feasible and would result in an extensive calibration effort. This paper therefore examines, on the basis of an experimental setup for automated endoscopic camera calibration, the extent to which certain calibration parameters can be modelled and approximated for each possible focal adjustment, and also investigates the influence of a liquid lens on the quality of the actual calibration.

Keywords: metrology, endoscopy, camera calibration, liquid lens

1. INTRODUCTION

By acquiring images and taking fluid or tissue samples from inside a person or organism, an endoscope is nowadays an indispensable diagnostic and manipulation tool in medical sector. In addition to purely diagnostic endoscopy, minimally invasive surgical procedures can be performed by combining it with various tools. This enables forms of treatment that are not feasible by other technical instruments and, accordingly, has a demonstrable impact on the mortality rates of various disease conditions.[1,2] Endoscopy embodies an innovative field, which opens up new applications and therapeutics or diagnostic methods through continuous technical improvement or synergies from other disciplines.[3] Endoscopes are also increasingly used in the technical and industrial context for the maintenance and inspection of areas or cavities that are difficult to access. On the one hand, this can support the quality assurance of various industries.[4] On the other hand, endoscopes are also increasingly used for maintenance purposes of critical equipment.[5]

Various types of endoscopes have been developed for a wide range of applications. In general, a distinction is made between rigid and flexible endoscopes, whereby rigid endoscopy is typically based on the Hopkins rod lens system, which has been continuously further developed since the 1960s which has led to a high degree of technical maturity. Due to the limitations of the range of motion of a rigid endoscope, flexible image guides have also been increasingly used for medical examinations since the 1970s, from which a wide variety of diagnostic disciplines or device classes, such as gastroscopes, coloscopes, bronchoscopes, and arthroscopes, have derived. Due to advancing camera miniaturization, another class of instruments, the so-called video endoscopes, emerged in the last two decades. The imaging optics and camera sensor are located directly in the measuring head, which enables more flexible guidance and reduced coupling-related losses by dispensing with optical image guides, but is currently still associated with the limitations of miniature cameras compared to conventional industrial cameras.

2. BACKGROUND

By means of a model-based camera calibration, it is possible to translate pixel information into world coordinates. In this context, the pinhole camera model is applied in a variety of different areas for the metric quantification of a scene. In case that the optical configuration remains unchanged, an accurate representation of the pixel information in world coordinates can be achieved with only a few parameters. Since no depth information can be derived from a flat pixel sensor, the pixel coordinates are transformed into three-dimensional beams. This means that in classical endoscopy, metric quantification of the scene can only be achieved by estimating the respective distance within the depth of field.

A second sensor enables a stereoscopic representation of the scene. Through the use of an additional calibrated camera, a three-dimensional point cloud can be obtained from the stereo image pair. The technical implementation of 3D endoscopy is mainly based on the principle of triangulation: By identifying homologous features within a stereoscopic system, three-dimensional information can be obtained from corresponding beams. Here, the photogrammetric approach is widely used in almost all commercially available systems. Two upper observation planes form a triangulation base. Using feature extraction, a three-dimensional reconstruction is performed from the stereo image pair via a disparity map.[6,7] This guarantees sufficient real-time capability, especially for moving measurement poses or measurement objects such as living organisms. A disadvantage of this approach is that it is purely passive and thus the information gain depends solely on the light emitted from the scene. Usually, therefore, these sensors are supplemented by an additional illumination fiber or one or more light sources in the measuring head. Nevertheless, the density of the reconstructed point cloud depends significantly on the texture of the specimen in order to match as many corresponding features in the stereo image pair as possible. In contrast, the active-triangulating endoscopic approach is currently the subject of further research. The projection of structured light onto the surface of the measured object not only opens up new fields of application, e.g. in an industrial context,[8,9] but also introduces a novel class of endoscopic instruments by providing high-resolution dense point clouds. An accurately calibrated camera and precise estimation of the triangulation base, i.e. position and orientation of the stereoscopic planes, is essential for sufficiently accurate triangulation.

3. PROBLEM DEFINITION

Endoscopic instruments are designed to be as compact as possible for application-related handling and therefore exhibit small apertures. In addition, imaging optics with small working distances and high magnifications are typically utilized. A major technical limitation in the use of endoscopic instruments is therefore posed by the depth of field (DOF). A 2D inspection or 3D triangulation can therefore only be performed in a small area and the instruments thus require frequent repositioning. Endoscopes with mechanical zoom are already commercially available, but have several limitations due to the mechanical actuation within the measuring head. The complexity of the assembly and the need for additional actuators, such as miniature motors, result in a larger measuring head size. In addition, a certain susceptibility to malfunctions results from the filigree optics and actuators, for example in the event of vibrations or mechanical shocks. A slow mechanical response as well as perceptible noises and high power consumption can also exclude possible applications.

In recent years, partially driven by the smartphone sector and the associated supply industry, another type of special optics - liquid lenses or fluid optics - has become available at comparatively low cost and in very compact designs. Liquid lenses typically consist of liquids of different densities. By applying an electric potential to opposing electrodes, electrostatic pressure causes the boundary layer between the two liquids to warp (electrowetting). Accordingly, the focus is adjusted in proportion to the applied potential.[10–12] Due to the fully electrical adjustment, very fast response and settling times can be realized and a significant increase of the depth of field is therefore feasible.

However, due to the strong influence of the fluid-optical focus variation on the optical configuration, it is expected that the camera parameters of a previously performed calibration lose their applicability and a new calibration must be conducted for an adequate reconstruction. Calibrating all adjusted focus positions results in impracticable effort and thus renders a practical application unlikely. This study is therefore dedicated to the investigation of the influence of a focus variation on the camera parameters in order to evaluate to what extent parameter interpolation is possible.
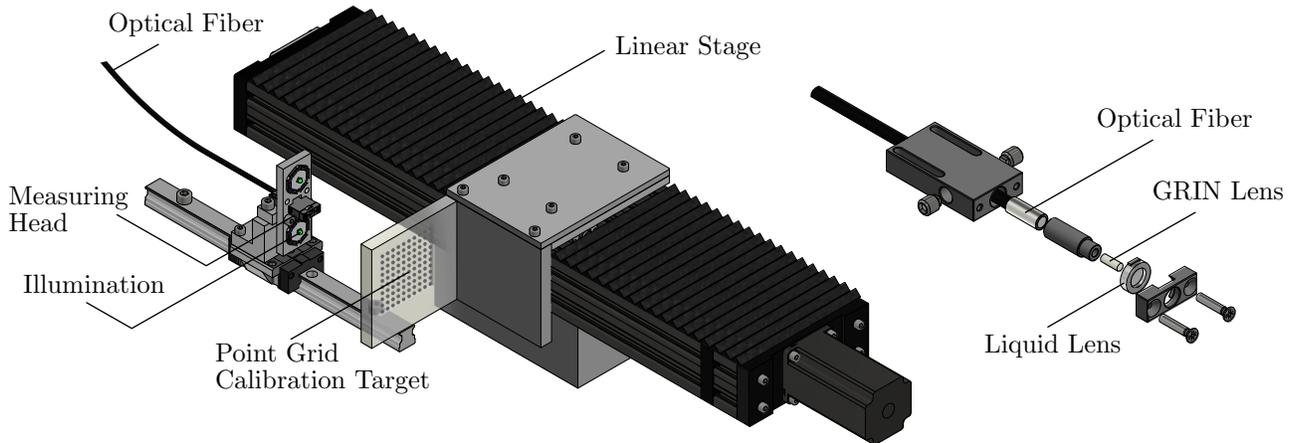
4. EXPERIMENTAL SETUP

Figure 1: Experimental setup at the measuring head end with all essential components and optics

The optical configuration of the fiber-optic coupling in this study, is essentially based on the work of Matthias[13] and Ohrt.[14] The applied monochromatic industrial camera of type GS3-U3-23S6M from FLIR Integrated Imaging Solutions Inc. (Wilsonwille, USA) is based on the IMX174 sensor from Sony Corporation (Minato, Japan) and is operated at a resolution of 1 184 px × 1 160 px at a selected gray scale resolution of 12 bit. The maximum sensor resolution is 1 920 px × 1 200 px with a pitch of the square pixels of 5.86 µm. The maximum frame rate is 162 fps. The fiber optic coupling is based on an infinity corrected objective lens at 10 × magnification and a numerical aperture (NA) of 0.25 supplied by Qioptiq Photonics GmbH & Co. KG (Göttingen, Germany) and a tube lens of 150 mm focal length. To prevent interference from stray light, the assembly is covered during the experiments. The applied fiber optic bundle of type FIGH-100-1500N from the manufacturer Fujikura Ltd. (Tokyo, Japan) has a length of 1 m and 100 000 individual fiber cores. The active area features a diameter of 1.4 mm with a NA of 0.4. A gradient index (grin) rod lens of type GT-IFRL-200-020-50-C1 from GRINTECH GmbH (Jena, Germany) with a working distance of 20 mm is applied to the measuring head as illustrated in figure 1. The diameter is 2 mm with a paraxial magnification of -10.87 and a field diameter of 15.2 mm. In addition, a focus-variable liquid lens of type A-16F from the manufacturer Corning, Inc. (New York, United States) with a clear aperture of 1.6 mm is integrated into the measuring head. The lens can be adjusted between -5 dpt and +15 dpt with an RMS wavefront error of 25 nm. The power consumption is 1 mW. The liquid lens is directly connected via a coaxial cable to a self-developed driver board (figure 2), which is mainly based on the HV892 driver from Microchip Technology Inc. (Chandler, United States). The other electrical components are based on the manufacturer's recommendations or provide data communication and power supply. A common 8-bit microcontroller is used for communication via the I^{2}C interface and for controlling the output. According to the manufacturer's specifications, the output of the HV892 can be adjusted in 256 individual steps via amplitude modulation between an RMS value of 9.8 V and 62.075 V. This could be confirmed experimentally and will serve as a measure for the corresponding focal
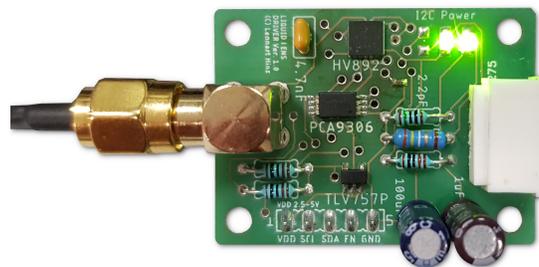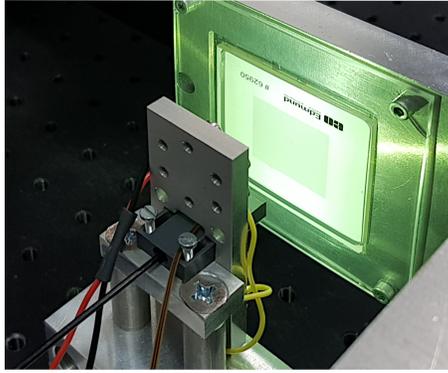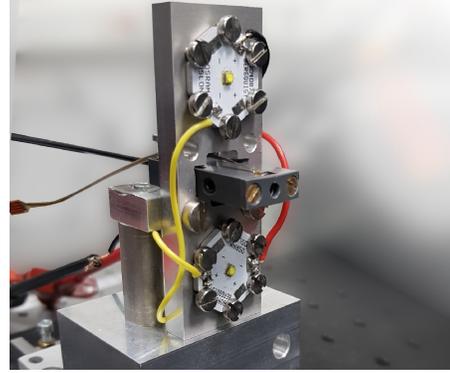

Figure 2: Driver board used for the generation of output levels

(a) Measurements on the calibration standard

(b) Measuring head holder with further external illumination

Figure 3: Overview of the prototypical measuring head with mounting and external illumination

setting in all further investigations. The output frequency is approximately 1.5 kHz. For the camera calibration, a diffuse reflective point grid pattern standard by Edmund Optics Inc. (Barrington, USA) of type #62-950 with a dot pitch of 250 µm is used. The positioning of this calibration standard is carried out via a motorized linear stage of type M-ILS50CC from the manufacturer Newport Corporation (Irvine, United States) with a guaranteed positioning accuracy of ±1.5 µm. Since the experiments of this study use an early, prototypical measuring head without illumination equipment, an external LED installation, as shown in figure 3, is implemented for optimal illumination of the calibration standard.

5. CALIBRATION PROCEDURE AND DATA PROCESSING

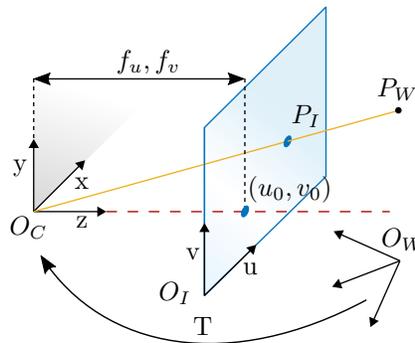## 5.1 Pinhole Camera Model and Distortion Correction

Figure 4: Overview of the pinhole camera model

The following section provides a basic overview of camera calibration and is mainly based on the relationships according to Hartley and Zissermann,[15] as well as the notation according to Heikkilä et al.[16]
Figure 4 shows a schematic overview of the pinhole camera model, which also represents the core of this study. A visible beam of a three-dimensional object point P_W in the world coordinate system O_W is imaged though a pinhole, represented by coordinate system O_C. The virtual image plane of a camera sensor with pixel image coordinate system O_I is intersected at the image point P_I.

$$w \begin{bmatrix} P_I \\ 1 \end{bmatrix} = KT \begin{bmatrix} P_W \\ 1 \end{bmatrix} \tag{1}$$

These relationships are expressed in equation 1, where the position t and orientation R of the world coordinate system O_W with respect to the pinhole or camera coordinate system O_C is defined via a three-dimensional

rigid transformation $T = [R, t]^T$. The relationship between the three-dimensional camera coordinates and the two-dimensional pixel coordinates is given by a projective transformation K. Where

$$K = \begin{bmatrix} f_u & 0 & 0 \\ s & f_v & 0 \\ u_0 & v_0 & 1 \end{bmatrix} \tag{2}$$

is also referred to as the camera matrix with intrinsic parameters and is composed of the focal lengths f_u and f_v, as well as the principal point (u_0, v_0). Since no depth information can be reconstructed from a two-dimensional image, equation 1 includes the additional scaling factor w. The skew factor s is not equal to zero if the axes of the coordinate system O_I are not perpendicular. For this study, perpendicular axes can be assumed. If the xy plane with respect to O_C and the uv plane with respect to O_I are parallel, $f_u = f_v$ applies. The ratio f_v/f_u of both focal lengths is also called aspect ratio and should accordingly be very close to 1. Since the intrinsic focal length is given in pixel coordinates, the pixel size or the pitch of the sensor needs to be multiplied for a transformation to world coordinates.

Since a pinhole camera cannot model lens properties, it is necessary to correct for distortion, especially due to the applied gradient index lenses. According to equation 3, normalized and distorted point coordinates $(u_{n,d}, v_{n,d})$ are calculated using the approach of Conrady[17] and Brown[18] (also known as the "Plumb Bob" model[19]). Where u_n and v_n are the image coordinates shifted to the image principal point (u_0, v_0) and normalized by the respective intrinsic focal length f_u and f_v. The radius r corresponds to the principal point in normalized coordinates and the coefficients $\{k_1, k_2, k_3\}$ specify radial distortion. It was found that 6th order radial distortion correction does not provide meaningful values for the optical configuration investigated here and is associated with considerable uncertainty. Accordingly, only a radial distortion correction of the second and fourth order is performed (analogous to Heikkilä et al.[16]) and $k_3 = 0$. Tangential distortion correction compensates for decentering and manufacturing imperfections, which is modeled by the coefficients p_1 and p_2.

$$\begin{bmatrix} u_{n,d} \\ v_{n,d} \end{bmatrix} = \underbrace{(1 + k_1 r^2 + k_2 r^4 + k_3 r^6) \begin{bmatrix} u_n \\ v_n \end{bmatrix}}_{\text{Radial Distortion}} + \underbrace{\begin{bmatrix} 2p_1 u_n v_n + p_2(r^2 + 2u_n^2) \\ p_1(r^2 + 2v_n^2 + 2p_2 u_n v_n) \end{bmatrix}}_{\text{Tangential Distortion}} \tag{3}$$

For a camera calibration it is therefore necessary to estimate the intrinsic camera matrix K, the extrinsic rigid body transformation T and the corresponding distortion coefficients $\{k_1, k_2, k_3, p_1, p_2\}$. The state of the art regarding calibration techniques and optimization algorithms is mainly based on the work of Zhang,[20] Tsai[21] and Heikkilä et al.[16] The investigations within the scope of this study are based on the toolbox of Bouguet.[22]

5.2 Calibration Procedure

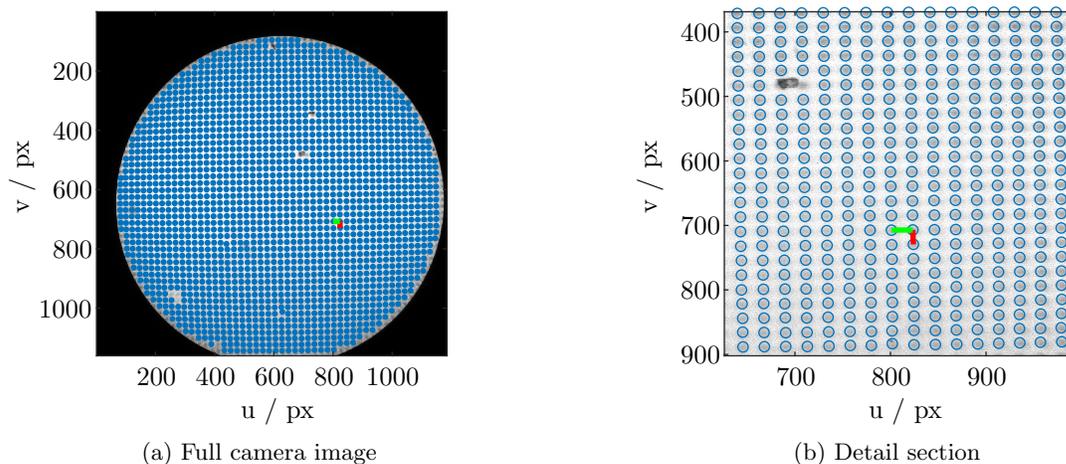(a) Full camera image

(b) Detail section

Figure 5: Extracted markers and reference coordinate system of an exemplary image

(a) All markers of a dataset   (b) Enlarged section   (c) Enlargement to a single feature
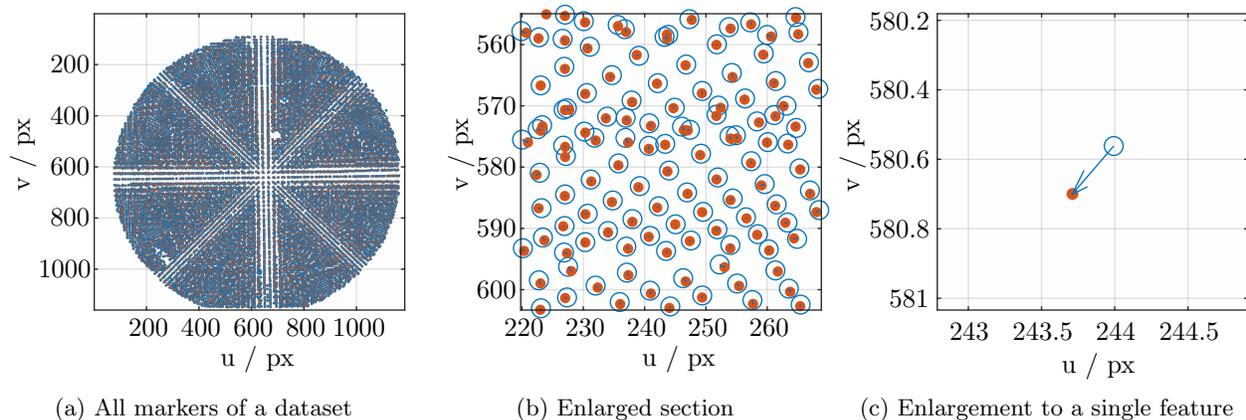
Figure 6: Reprojection error (blue arrow) of all calibrated features of an exemplary calibration dataset

A geometric calibration target with multiple markers at a defined distance and a known geometric arrangement are typically used to approximate the given parameters when positioned at different poses. For a accurate and robust calibration, an unambiguous estimation of each marker position with respect to the world coordinate system O_W is necessary. Therefore, calibration targets with given coordinate systems are usually used, or a fixed, easily identifiable marker (such as a specific corner point) serves as the coordinate origin. Due to the endoscopic setup, a point grid standard (see section 4) is used for camera calibration. Since no identifiable coordinate system exists on the standard, feature tracking is necessary for robust marker extraction. In combination with the linear stage, a reference feature, which serves as the world coordinate system, is thus tracked while the target is moved through the depth of field. For this, it is important that the step size is smaller than half the marker pitch. For more information on the algorithms of the marker extraction pipeline and the calibration approach, reference is made to the work of Matthias,[13] which is used in the investigations of this study with a few modifications. Figure 5 shows an example of the extracted markers and the selected coordinate system at a specific focus adjustment and linear stage position. In order to correct the results of this study of stochastic influences and erroneous calibrations, 10 individual calibrations are performed for each focus adjustment by tracking different reference markers. For this purpose, random, reference markers are identified by normally distributed reference start values which are generated in the estimated middle area of the glass fiber with a standard deviation of 150 Pixels. Figure 5 indicates that due to slight misalignment, the center of the glass fiber deviates from the center of the image, which, however, is irrelevant for all further investigations, and only a very small edge area is cut off. Due

(a) After the first calibration   (b) After outlier removal and final calibration
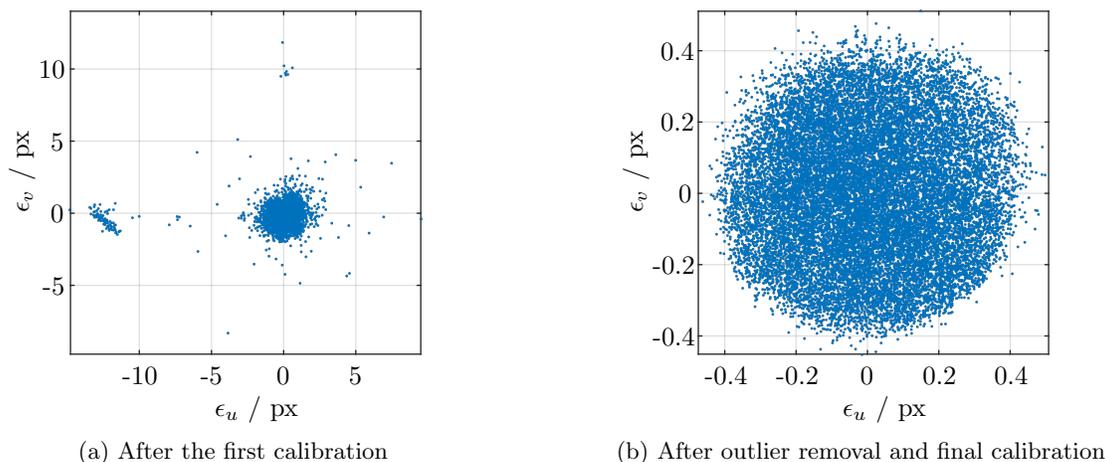
Figure 7: Location of the reprojection errors of all extracted features of an exemplary dataset

to the focus adjustment, a larger range has to be travelled by the linear stage including positions outside the respective depth of field. Since marker tracking and thus camera calibration is not possible outside the depth of field, the image stack to be processed is first reduced to focused images. For this purpose, only those images are selected in which at least 25 % of the maximum number of markers of the respective focus adjustment has been detected. The extracted markers are then applied for camera calibration according to the pinhole camera model. Accordingly, the reprojection error in pixel coordinates (ϵ_u, ϵ_v) is calculated for each feature and then globally minimized. The reprojection error is shown for an exemplary dataset in figure 6 for three different detail levels and quantifies the deviation of the model-based (blue circle) from the measured (orange dot) feature position. If no systematic errors are present, the reprojection error ϵ should be evenly distributed. Figure 7a shows that there are certain outliers after a calibration has been performed. Figure 5b indicates that possible outliers are caused by dirt particles, for example. Therefore, in a second step, 25 % of the extracted markers with the largest reprojection error are discarded and the calibration is performed again (figure 7b).

6. RESULTS

In the following, the main results of this study will be presented. The focus is given by the influence of the lens adjustment on the respective camera parameters. The repeatability of the lens adjustment is also reflected by the following results, but was not investigated in further detail in the conducted experiments.

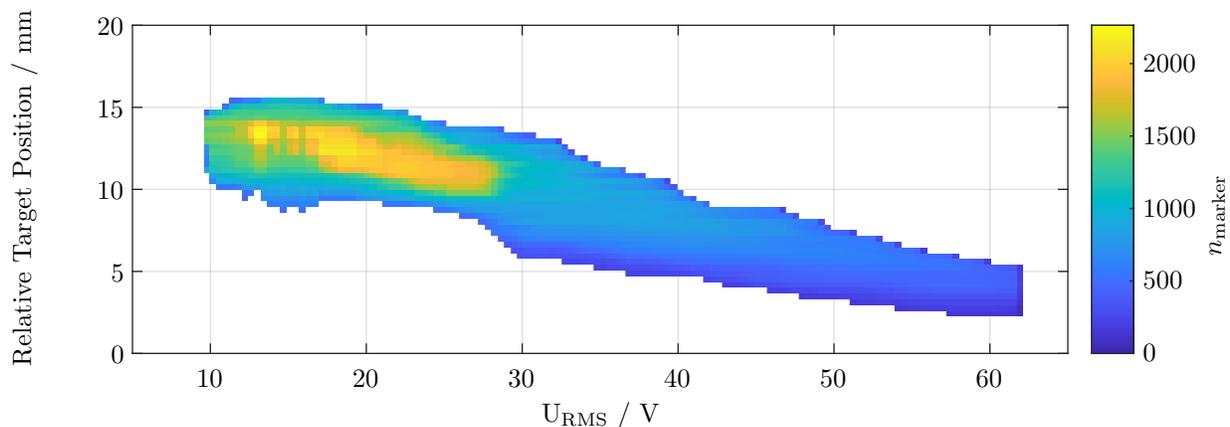### 6.1 Limiting the Depth of Field and Error Considerations

Figure 8: Position of DOF and number of extracted markers with respect to each focus adjustment

Figure 8 shows the relative linear stage position with the number of extracted markers for subsequent calibration versus focus adjustment respectively RMS voltage. It is noticeable that in the range of about 10 V $\leq$ U$_{\mathrm{RMS}}$ $\leq$ 30 V, significantly more markers are extracted. For U$_{\mathrm{RMS}}$ > 30 V the usable depth of field range widens significantly. For higher voltages however, the depth of field becomes narrower again.

Figure 9 shows the boxplots of all performed calibrations for the corresponding focus adjustment with respect to the euclidean norm of the standard deviations of the remaining reprojection errors. It is noticeable that especially in the range with the high number of markers, the calibrations are affected significantly by irregularities. This is counterintuitive, since in principle a more robust calibration can be assumed with an increasing number of markers. The manufacturer specifies an operating range of 36.5 V $\leq$ U$_{\mathrm{RMS}}$ $\leq$ 54.5 V for the adjustable lens. The transition from scattering to focusing properties is specified at U$_{\mathrm{RMS}}$ = 42 V. It is therefore possible that the negative focal length initially results in more markers being found in the image section. However, these may be too small to be tracked robustly at every start value constellation. Figure 10 shows the minimum error of a set of calibrations of a respective focus adjustment. It can be seen that a calibration basically works for all focus adjustments and provides comparable error ranges. This also applies well outside the working range specified by

the manufacturer. In order to correct the results of the experiments from possible erroneous calibrations, only the calibrations with the lowest error value for each focus adjustment are compared in the following.
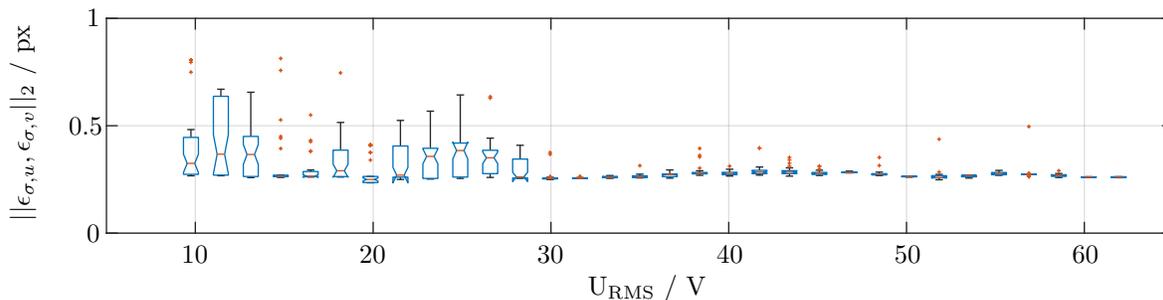

Figure 9: Boxplot of the euclidean norm of the standard deviation of all reprojection errors for each focus adjustment
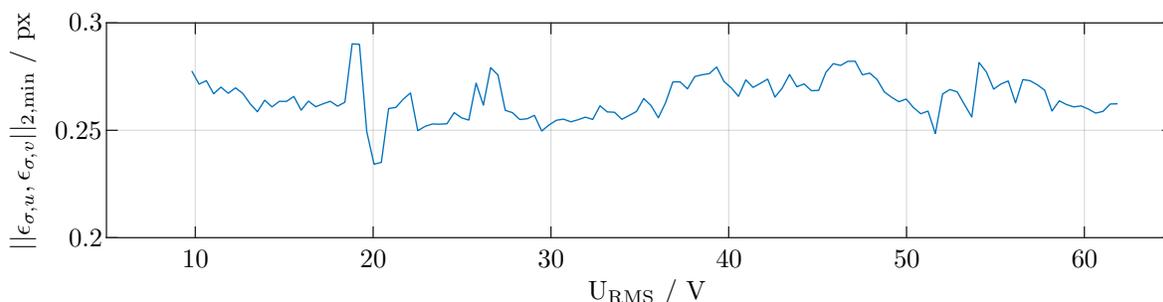

Figure 10: Minimum of the norm of the standard deviation of all reprojection errors for each focus adjustment

6.2 Intrinsic Calibration
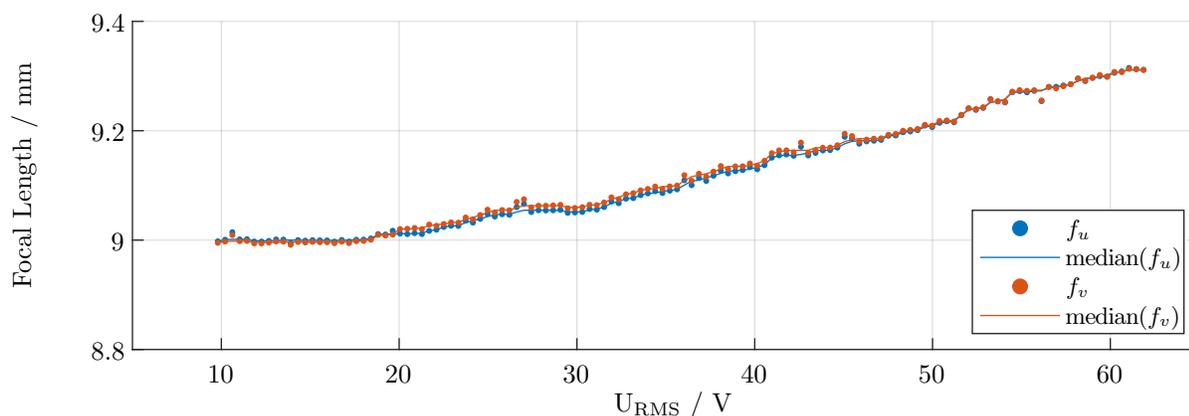
6.2.1 Focal Length

Figure 11: Intrinsical focal lengths (in world coordinates) for each focus adjustment

Figure 11 shows the relationship between the focal length (in world coordinates) of the projective 2D to 3D correspondence and the respective focus adjustment. Especially at $U_{RMS} \geq 30$ V a good linearity can be observed.
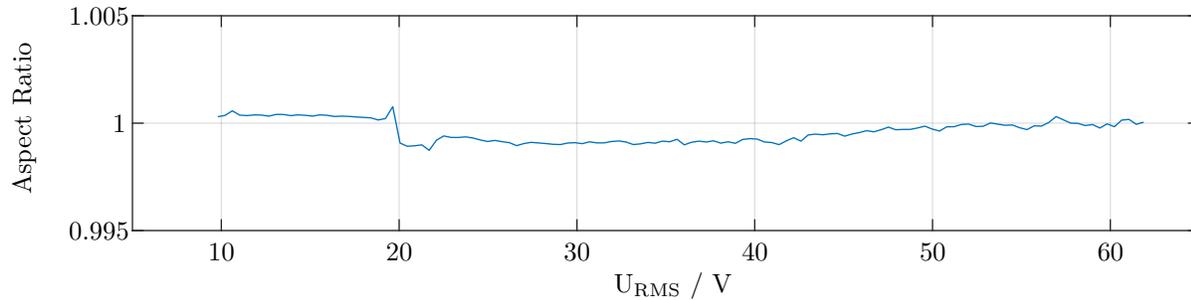
Figure 12: Aspect ratio for each focus adjustment

It is noticeable that the transition from negative to positive optical power ($U_{RMS} = 42$ V) is very smooth and cannot be determined from the presented data since it relates to the focal length of the combined endoscopic system. At $U_{RMS} \leq 20$ V, the calibrated focal length does not seem to change with the applied voltage. This is consistent with the manufacturer's specifications. A deviation of both focal lengths is noticeable at 20 V $\leq U_{RMS} \leq 50$ V, indicating slight astigmatism. This is also shown in the aspect ratio according to 12. A model-based drift can be excluded, since each calibration is independent with its own data set and different reference markers. However, the deviations are so small that they probably have no quantifiable influence.
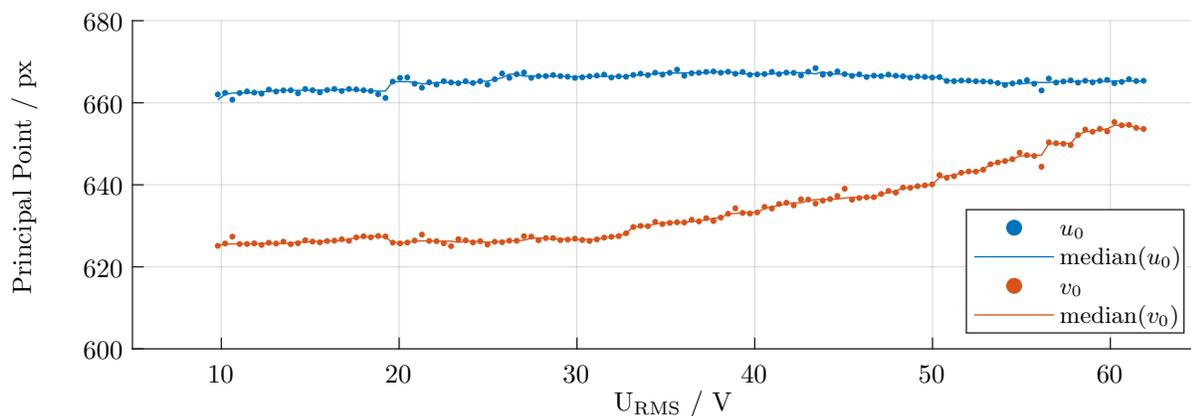
6.2.2 Principal Point

Figure 13: Coordinate of the principal point for each focus adjustment

Figure 13 shows the influence on the position of the principal image point as a function of the adjusted focus. It is noticeable that only the vertical component v_0 is influenced by a focus variation. In accordance to the focal length, a proportionality can be observed from a voltage of $U_{RMS} \geq 30$ V. The shift of approx. 30 px is small, but should be taken into account in any case. Possibly this influence is rather due to adjustment and can be reduced in further constructive improvements.

6.3 Distortion Correction
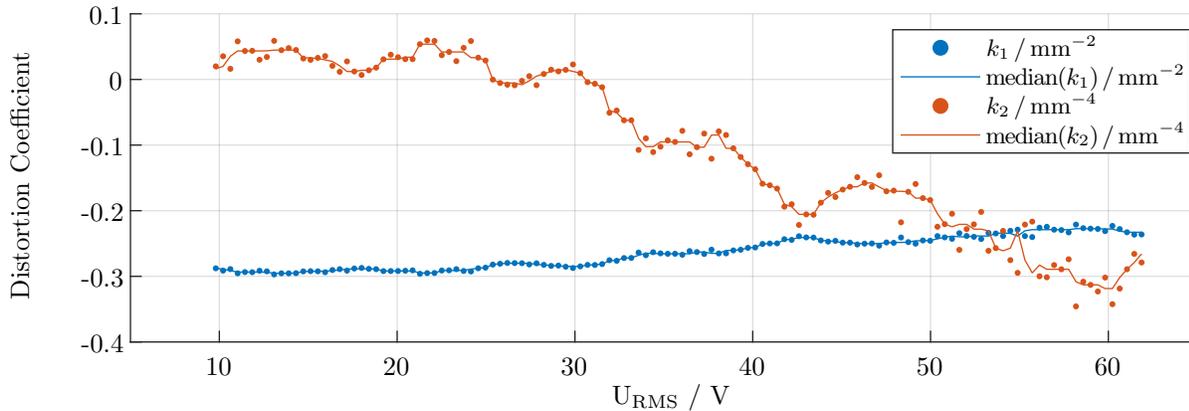
6.3.1 Radial Distortion

Figure 14: Coefficients of radial distortion with respect to each focus adjustment

Figure 14 shows the radial distortion coefficients as a function of the adjusted focus. For better interpretation, the displacement is visualized in figure 15 for $U_{RMS} \approx 10$ V and $U_{RMS} \approx 65$ V. Figure 15 additionally shows the center of the image (cross) and the current principal point of the respective calibration (circle). Note that the direction of the Y-axis is reversed compared to figure 13 and the principal point therefore moves downwards. The 2nd radial order (k_1) increases slightly, while the 4th radial order (k_2) exhibits a clear, negative proportionality as well as stronger noise. Within certain limits, linearity can be assumed, which again excludes smaller voltages ($U_{RMS} \leq 25$ V) values from applicability.

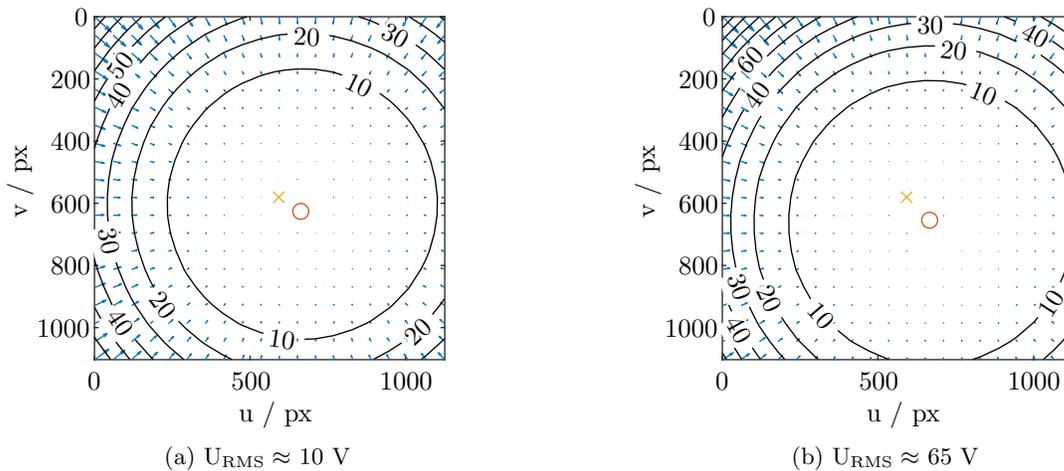(a) $U_{RMS} \approx 10$ V

(b) $U_{RMS} \approx 65$ V

Figure 15: Visualization of the displacement due to radial distortion for two exemplary focus adjustments
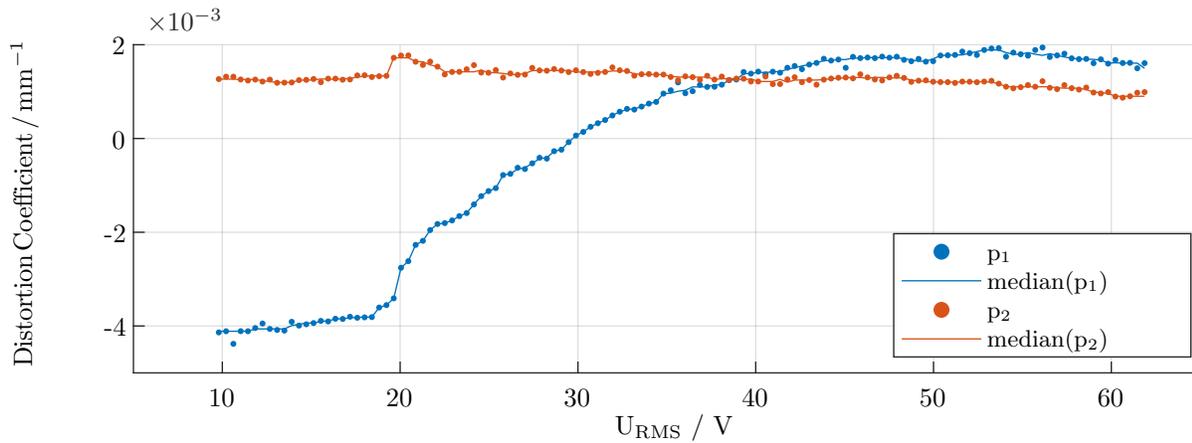
6.3.2 Tangential Distortion

Figure 16: Coefficients of tangential distortion with respect to each focus adjustment

Figures 16 and 17 show the relations for the two tangential distortion coefficients. First of all, it is noticeable that the absolute displacement is significantly lower compared to the radial distortion and has only a very small influence on the resulting combined distortion (see equation 3). This may be due to a good mechanical adjustment and high quality of the optical components. However, there is a clear influence of the distortion for $U_{RMS} \geq 20$ V. Especially for the coefficient p_1, this effect is certainly not linear, while linearity can probably be assumed for p_2.
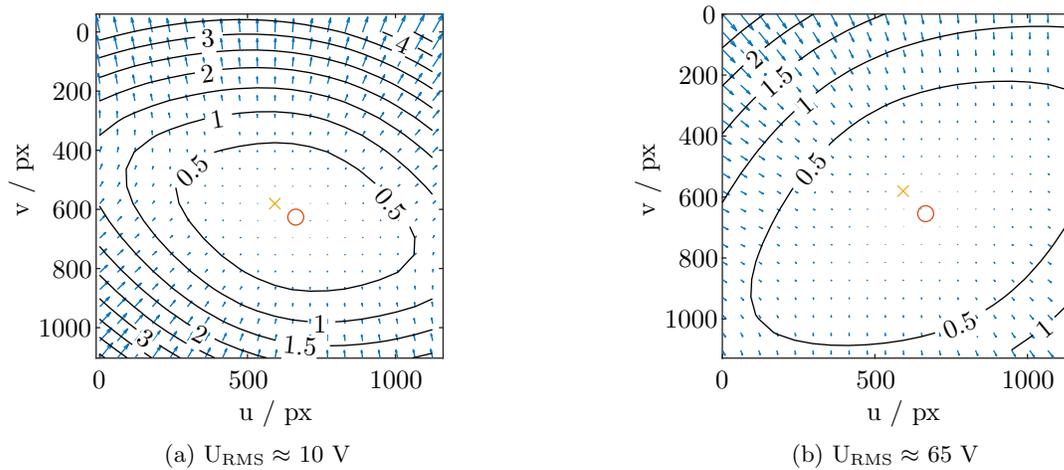

(a) $U_{RMS} \approx 10$ V

(b) $U_{RMS} \approx 65$ V

Figure 17: Visualization of the displacement due to tangential distortion for two exemplary focus adjustments
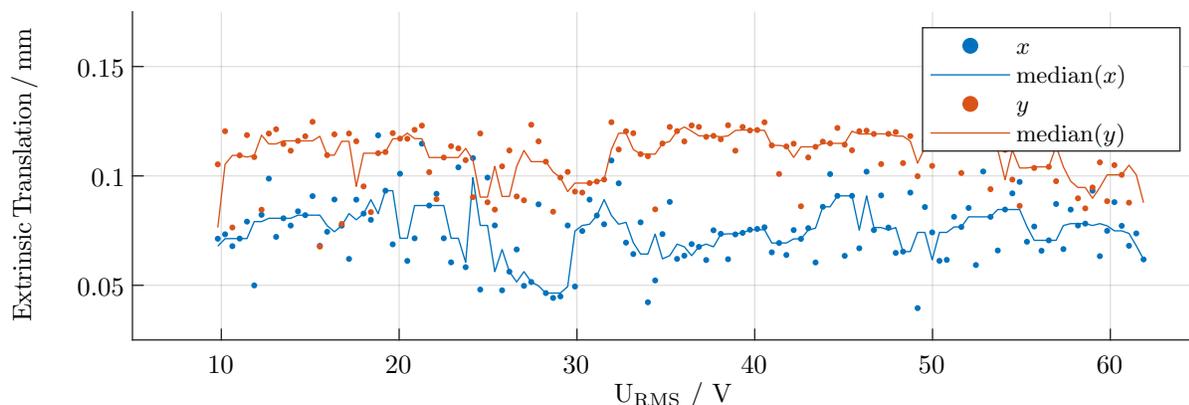
6.4 Extrinsic Calibration

6.4.1 Translation

Figure 18: x and y components of the extrinsic translation for each focus adjustment

Figure 18 shows the x and y components of the extrinsic translation as a function of the adjusted focus. Since the reference coordinate system is placed in a randomly chosen reference marker, the translation components were shifted by integer multiples of the point spacing of the calibration standard grid. Basically, both components are not affected by the voltage applied to the liquid lens. However, with a standard deviation of 15.4 μm for the x component and 12.8 μm for the y component, some amount of variation is present and should be investigated in further experiments. Figure 19 refers to the z component of the extrinsic translation. If the aspect ratio is approximately 1, there should be parallelism to the optical axis of the camera coordinate system and no influence of marker ambiguity. Despite some possible, minimal astigmatism, this seems to be the case, since overall good proportionality can be observed. It is also noticeable that a linearity prevails across all voltages and is not limited to certain ranges. Across the full focus range, the focal length has increased by about 0.3 mm (see section 6.2.1), while the z coordinate of the extrinsic translation has decreased by about the same value. This implies that for increasing voltage values U_{RMS}, the pinhole or camera coordinate system O_C approaches the image plane of the sensor.
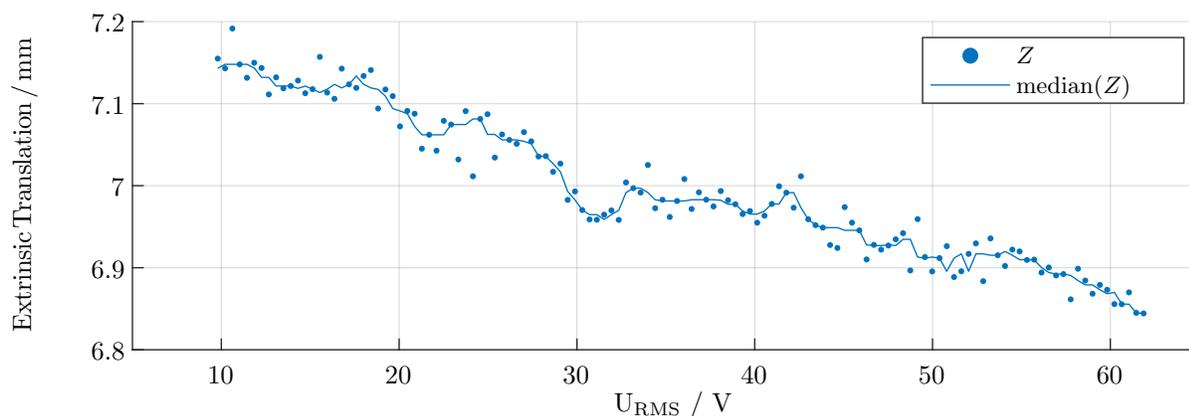

Figure 19: z component of the extrinsic translation for each focus adjustment
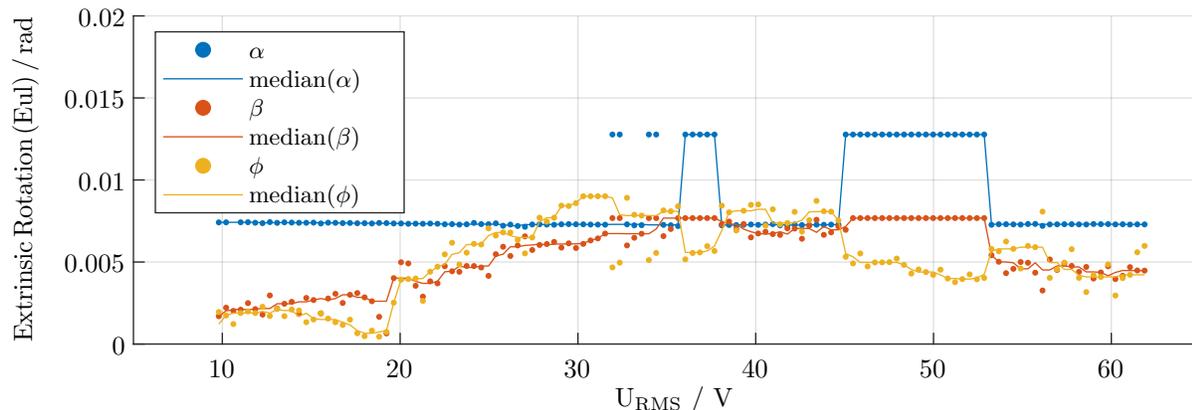
6.4.2 Rotation

Figure 20: Representation (in Euler angles) of the extrinsic rotation for each focus adjustment

Figure 20 shows the orientation of the extrinsic calibration (in Euler angles) as a function of the adjusted focus. Since the orientation of the coordinate system can also be different for each calibration, the respective angles were adjusted for 90° jumps. These jumps can be observed in particular for α. Overall, the fluctuations of all three angles are so small that constant behavior can probably be assumed.

7. CONCLUSION

The investigations carried out in this study demonstrate that the use of the pinhole camera model for an endoscope with a adjustable liquid lens is feasible. Especially in the working range specified by the manufacturer, it is possible to consider many parameters as linear or constant and to interpolate them with only a few support points. This effectively minimizes the experimental and computational effort from many hours to a few minutes and is a useful way of enabling practical applications. The calibration procedure also provides reproducible parameters. Nonlinearities such as those in the area of tangential distortion have a very small influence and are presumably dependent on the adjustment and therefore tend to behave differently.

The investigations have also shown that, especially for positive optical power, it is possible to use the adjustable lens beyond the specified ranges. For the presence of negative optical power, the results are less promising. This is mainly due to the fact that in this focal range the marker extraction algorithm is prone to errors and the observed proportionalities do not seem to be valid.

8. FURTHER RESEARCH

Based on this study, further improvements are conceivable and complementary experiments can be conducted. It has been shown that the marker extraction algorithm is prone to errors for certain focus adjustments. This applies in particular to the range 20 V $\leq$ U$_{\text{RMS}}$ $\leq$ 30 V, since the focal length already increases linearly here, but many calibrations lead to erroneous results. It is important to investigate to what extent a different calibration standard and algorithmic improvements can compensate for this. In this way, the overall feature tracking can be further improved, including in particular the random selection of reference marks from the center of the image. For triangulation-based measurement systems, which require a clearly and precisely identified triangulation base, ambiguities with regard to the position and orientation of the world coordinate system are disadvantageous. An unambiguous and reproducible extrinsic reference coordinate system, independent of the focus adjustment, should therefore be aimed for in a revision of marker tracking.

Furthermore, it is necessary to quantify the error by the parameter approximation with a limited number of support points and to define given limits. Here, the reprojection error can be used as a benchmark, although other metrics are also conceivable depending on the specific application.

The measuring head introduced in this study is rather prototypical and serves the evaluation of the optical

configuration. Significant miniaturizations, as well as the combination with an illumination unit are possible. In this context, a incident light illumination ring or a coaxial illumination approach can be investigated. Although the latter is significantly more compact, the fiber optic coupling and the narrow apertures possibly result in poorer illumination. Therefore, these two illumination concepts shall be weighed against each other in further studies.

ACKNOWLEDGMENTS

REFERENCES

[1] Muller, A. D., "Prevention of colorectal cancer by flexible endoscopy and polypectomy: A case-control study of 32 702 veterans," *Annals of Internal Medicine* **123**, 904 (dec 1995).

[2] Nishihara, R., Wu, K., Lochhead, P., Morikawa, T., Liao, X., Qian, Z. R., Inamura, K., Kim, S. A., Kuchiba, A., Yamauchi, M., Imamura, Y., Willett, W. C., Rosner, B. A., Fuchs, C. S., Giovannucci, E., Ogino, S., and Chan, A. T., "Long-term colorectal-cancer incidence and mortality after lower endoscopy," *New England Journal of Medicine* **369**, 1095–1105 (sep 2013).

[3] Cho, J. E., Shamshirsaz, A. H. A., Nezhat, C., Nezhat, C., and Nezhat, F., "New technologies for reproductive medicine: laparoscopy, endoscopy, robotic surgery and gynecology. a review of the literature.," *Minerva ginecologica* **62**, 137–167 (Apr. 2010).

[4] Puliparambil, J. T., Gilbert, J. A., and Matthys, D. R., "Endoscopic inspection using a panoramic annular lens," in [*Second International Conference on Photomechanics and Speckle Metrology*], SPIE (dec 1991).

[5] Hofmann, A., Albertazzi, A., Santos, J. C., Valim, E., Gondo, R., and Freitas, T., "A stereoscopic endoscopic optical system for measurement of the 3d weld geometry of pipes: Concepts and preliminary results," in [*Volume 4: Terry Jones Pipeline Technology; Ocean Space Utilization; CFD and VIV Symposium*], ASMEDC (jan 2006).

[6] Thormahlen, T., Broszio, H., and Meier, P., "Three-dimensional endoscopy," (02 2003).

[7] Zhou, J., Zhang, Q., Li, B., and Das, A., "Synthesis of stereoscopic views from monocular endoscopic videos," in [*2010 IEEE Computer Society Conference on Computer Vision and Pattern Recognition - Workshops*], IEEE (jun 2010).

[8] Ohrt, C., Pösch, A., Kästner, M., and Reithmeier, E., "Potentials of endoscopic fringe projection – a differentiation of measuring video-, fiber- and borescopy," in [*Fringe 2013*], 735–740, Springer Berlin Heidelberg (2014).

[9] Schick, A., Forster, F., and Stockmann, M., "3d measuring in the field of endoscopy," in [*Optical Measurement Systems for Industrial Inspection VII*], Lehmann, P. H., Osten, W., and Gastinger, K., eds., SPIE (may 2011).

[10] Ren, H. and Wu, S.-T., "Variable-focus liquid lens," *Optics Express* **15**, 5931 (apr 2007).

[11] Kuiper, S. and Hendriks, B. H. W., "Variable-focus liquid lens for miniature cameras," *Applied Physics Letters* **85**, 1128–1130 (aug 2004).

[12] Cheng, C.-C. and Yeh, J. A., "Dielectrically actuated liquid lens," *Optics Express* **15**, 7140 (may 2007).

[13] Matthias, S., "A flexible endoscopic structured light 3-d sensor: Design, models and image processing," (2018).

[14] Ohrt, C., [*Development of a measuring endoscope for the in-line quality control of filigree form elements in forming production lines*], PZH-Verlag (2014).

[15] Richard Hartley, A. Z., [*Multiple View Geom Comp Vision 2ed*], Cambridge University Press (2019).

[16] Heikkila, J. and Silven, O., "A four-step camera calibration procedure with implicit image correction," in [*Proceedings of IEEE Computer Society Conference on Computer Vision and Pattern Recognition*], IEEE Comput. Soc (1997).

[17] Conrady, A. E., "Decentred lens-systems," *Monthly Notices of the Royal Astronomical Society* **79**, 384–390 (mar 1919).

[18] Brown, D. C., "Close-range camera calibration," *Photogrammetric Engineering* **37**(8), 855–866 (1971).

[19] Brown, D. C., "Decentering the distortion of lenses," *Photogrammetric Engineering* **32**, 444–462 (01 1966).

[20] Zhang, Z., "A flexible new technique for camera calibration," *IEEE Transactions on Pattern Analysis and Machine Intelligence* **22**(11), 1330–1334 (2000).

[21] Tsai, R., "A versatile camera calibration technique for high-accuracy 3d machine vision metrology using off-the-shelf TV cameras and lenses," *IEEE Journal on Robotics and Automation* **3**, 323–344 (aug 1987).

[22] Bouguet, J.-Y., "Camera calibration toolbox for matlab," (2015).